Advanced Powder Technology 34 (2023) 104106

Contents lists available at ScienceDirect

Advanced Powder Technology

journal homepage: www.elsevier.com/locate/apt

Discrete element modeling of granular hopper flow of irregular-shaped deformable particles

Zhengshou Lai [a], Yidong Xia [b,*], Qiushi Chen [c,*]

[a] School of Civil Engineering, Sun Yat-sen University, Zhuhai 519082, China
[b] Energy and Environment Science & Technology Directorate, Idaho National Laboratory, Idaho Falls, ID 83415, USA
[c] Glenn Department of Civil Engineering, Clemson University, Clemson, SC 29634, USA

ARTICLE INFO

Article history:
Received 2 March 2023
Received in revised form 25 April 2023
Accepted 27 May 2023

Keywords:
Discrete element method
Hopper flow
Deformable particles
Flow characteristics
Discharge rate

ABSTRACT

Many natural and engineered granular materials have relatively deformable particles. Besides particle size and shape, particle deformability is another salient factor that significantly impacts the material's flow behavior. In this work, the flow of irregular-shaped deformable particles in a wedge-shaped hopper is investigated using discrete element simulations. A bonded-sphere model is developed to simultaneously capture irregular particle shapes and particle-wise deformations (e.g., compression, deflection, and distortion). Quantitative analysis of the effects of irregular shapes and particle deformations shows that the increase in particle stiffness tends to increase initial packing porosity and decrease the flow rate in the hopper. Rigid particles tend to have clogging issues, whereas deformable particles have less chance to, indicating particle deformation reduces the critical bridging width in the hopper flow. Detailed analysis of stress fields is also conducted to provide insights into the mechanism of particle flow and clogging. Stresses and discharge rates calculated from numerical simulations are compared and show good agreement with Walker's theory and the extended Beverloo formula. Simulations with various particle shape combinations are also performed and show that the initial packing porosity decreases with an increasing percentage of fibers while the discharge rate has a complex dependency on particle shapes.

1. Introduction

Hoppers are wedge- or cone-shaped bins used for storing and discharging granular materials. They are widely used in many industries such as mining, food, chemicals, agriculture and manufacturing. Although most hoppers are simple in geometric configurations, the discharge flow dynamics can be complicated due to the influence of various factors related to the geometry of the hopper and the characteristics of the flow media. Hopper design is critical because inappropriate design can result in poor operation performance and even equipment or functionality issues (e.g., clogging and ratholing) [1]. Therefore, great efforts, including both experimental and numerical efforts, have been and will continue to be made to better understand granular hopper flow.

Due to the discrete nature of granular materials, the particle-based discrete element method (DEM) [2] has emerged as the most preferred numerical tool for modeling granular hopper flow and understanding the flow behavior based on the micromechanics of granular materials. There have been a plethora of DEM-based numerical studies on granular hopper flow over the past two decades. Some of the previous studies focused on investigating the intrinsic characteristics of granular hopper flows, such as stresses in the flow media and on the hopper wall [3,4], flow patterns (e.g., mass flow vs. funnel flow) [5,6], flow dynamics and fluctuations [7–9], and the segregation behavior [10,11]. Other research put more emphasis on the effects of hopper geometry on the flow behavior, including hopper shapes [12] and orifice sizes [13]. The effect of material attributes and particle-scale parameters on the flow behavior has also been an important consideration in recent DEM-based studies [3,14–20]. Parametric studies on the contact stiffness [3], the particle–particle contact friction [3,15], and the particle–wall contact friction [21] have been conducted to gain insights into the sensitivity of granular hopper flow to the microscopic contact parameters. In terms of modeling and quantifying effects of irregular particle shapes, super-quadrics [14], clumps of overlapping spheres [16,17], and ellipsoids [18] have been proposed and employed in DEM simulations of granular hopper flows.

The aforementioned DEM-based numerical studies of granular hopper flow considered and modeled individual particles as rigid

* Corresponding authors.
E-mail addresses: yidong.xia@inl.gov (Y. Xia), qiushi@clemson.edu (Q. Chen).

https://doi.org/10.1016/j.apt.2023.104106

bodies without any particle-wise deformations (e.g., compression, deflection or distortion). For granular materials with relatively rigid particles (e.g., sand and pharmaceutical pills), such consideration works well, and particle sizes and shapes are known to be the primary factors affecting their mechanical behavior and flowability [14,22]. However, many natural and engineered granular materials, such as woodchips, corn stover, and switchgrass, have constituent particles that may exhibit substantial deformations even under low external loads [23–25]. In addition to particle sizes and shapes, particle deformation is another important factor that should be accounted for when studying the flowability of these materials. Therefore, although granular hopper flows of different scenarios have been extensively studied via DEM, the observations and conclusions from these previous studies suit only rigid particle flows and may not be applicable to flow of irregular-shaped deformable particles.

To account for deformations of irregular-shaped particles in DEM, the prevalent approach in recent years is to employ the bonded-particle model, which was initially devised by Potyondy and Cundall [26] to model fracture initiation and evolution across mineral grains in rocks. In the bonded-particle model, an irregular-shaped deformable particle is represented by a cluster of base elements such as spheres [27], cylinders [26,28], and sphero-cylinders [29]. The base elements are connected by bonds (or joints), on which bond models are imposed to transfer forces and moments. Bonded-particle DEM models have been developed and applied to investigate the packing [29], compression [30,31], and shear flow behavior [27] of flexible fibers, the separation of grain-straw mixtures [28], and the mechanical behavior of biomass feedstocks [32–35]. However, the granular flow of irregular-shaped deformable particles, which has wide applications in biomass logistics and biorefinery processes [36–38], remains a topic less explored. Key knowledge gaps exist in modeling the hopper flow of such materials and in understanding the effects of irregular shapes and particle deformations on the hopper flow behavior.

Besides the bonded-particle approach for modeling deformable particles, other approaches also exist to model deformable particles as a single object and employ analytical or numerical methods to evaluate its deformation. For example, Zhou et al. [39] discretized the surface of a particle into a set of pseudo nodes and particle deformation is achieved by the update of velocities and positions of the pseudo surface nodes according to accurate force analysis. Rojek et al. [40] considered that a particle is subjected to a uniform stress field, which is estimated from all the contact forces subjected by the particle. The strain could be then calculated and the particle deformation is obtained by integration of the particle strain. Cantor et al. [41] and Vu et al. [42] adopted the finite element method to simulate the deformation of a particle. In a similar fashion, the material point method was adopted by Nezamabadi et al. [43] for modeling the compaction of plastic particle packings. The advantages and disadvantages of those approaches vary regarding their accuracy and computational efficiency.

The primary goal of this work is to develop a DEM-based approach to model and investigate granular hopper flow with the capability of embodying different particle sizes, irregular particle shapes, and more importantly, particle deformations. For this purpose, a bonded-sphere model is developed to represent irregular-shaped deformable particles in DEM. Loblolly pine woodchips are the deformable granular materials used for conceptualizing irregular shape templates and calibrating the contact parameters in the DEM model. As a major contribution, the flow characteristics of irregular-shaped deformable particles in a wedge-shaped hopper are analyzed in details and compared with those of spherical particles and rigid particles. The particle and wall stresses are also compared with Walker's theory and the discharge rate are benchmarked against the extended Beverloo formula. To further understand the effects of particle shapes and deformations, parametric studies on the particle bond stiffness and shape combinations are carried out. The analysis and findings demonstrate the importance of particle deformation effects. The methodology and workflow presented in this study can be conveniently extended to model and study granular flows of hoppers with different geometries and with particles of wider variations in size, shape, and deformability.

The remainder of the paper is structured as follows: Section 2 presents the formulation of the bonded-sphere DEM model for irregular-shaped deformable particles. The model is then used to set up granular hopper flow tests detailed in Section 3. Section 4 presents simulation results and detailed analysis on the effects of irregular shapes and particle deformations on flow characteristics. The conclusions of the present study are summarized in Section 5.

2. Bonded-sphere DEM model

In this section, we present the formulation of the bonded-sphere model for the representation of irregular-shaped deformable particles in DEM. For completeness, DEM basics and the adopted inter-particle contact model are also briefly described.

2.1. Bonded-sphere model for deformable particles

In the bonded-sphere model, spheres are used as the base elements and are connected by bonds (or joints) to form clusters that represent irregular-shaped deformable particles. In this work, we use the term "particle" to refer to a cluster of bonded spheres. Fig. 1 shows the sketch of the bonded-sphere model and its rheological components. In this model, multiple spheres (e.g., two spheres shown in Fig. 1) connected by bonds form a "particle". Bonds can be regarded as special contacts that carry forces and moments, allowing the connected spheres to have relative displacements when subject to external loads. The deformation of the particle is then reproduced from the overall effects of relative displacements between the spheres within the particle. To describe the bond behavior between base spheres, the linear parallel bond model [26] is adopted in this study. It is a simple yet effective model that can describe both the relative translational and rotational displacements of bonded spheres. More complicated bond models such as the rolling resistance model [44–46], the elasto-plastic model [47,34], and the visco-elasto-plastic constitutive model [48], can also be used to accommodate the modeling needs of specific materials.

As shown in Fig. 1, in the linear parallel bond model, the bond between two spheres is assumed to be a cylinder of finite radius and thickness. Each point in the bond is imposed by two linear elastic springs providing normal and shear resistances, respectively. The overall bonding force and moment are the integral of the normal and shear stresses at the cross-section of the bond. In the calculation, the bond force $\vec{F}^b$ is separated into two parts: normal force F_n^b and shear force F_s^b; and the bond moment $\vec{M}^b$ is also separated into two parts: twisting moment M_n^b and swinging moment M_s^b. The incremental form of these components can be written as [26]

$$\Delta F_n^b = k_n^b A \Delta\delta_n \tag{1}$$

$$\Delta F_s^b = k_s^b A \Delta\delta_s \tag{2}$$

$$\Delta M_n^b = k_s^b J \Delta\theta_n \tag{3}$$

$$\Delta M_s^b = k_n^b I \Delta\theta_s \tag{4}$$

where $\delta_n, \delta_s, \theta_n$ and θ_s are the relative normal displacement, shear displacement, twisting rotation, and swinging rotation between

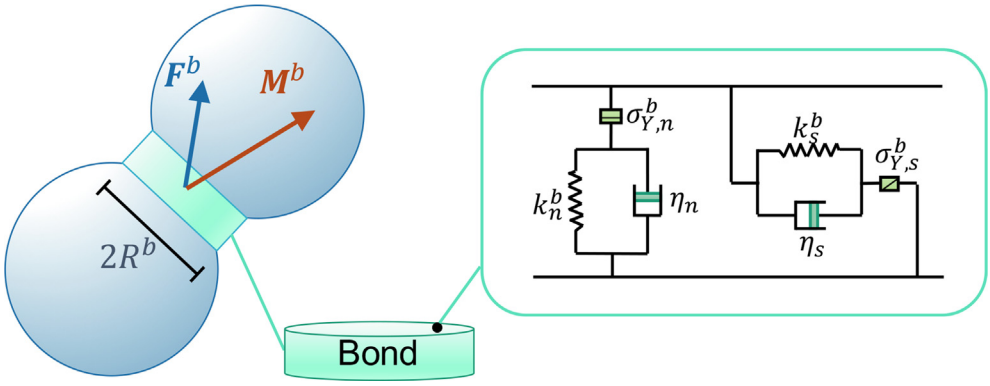

Fig. 1. Sketch of the bonded-sphere model and its rheological components (symbols explained in the main text).

the two bonded spheres, respectively; A, I, and J are the area, the moment of inertia, and the polar moment of inertia of the bond (i.e., the bond cross-section with radius R^b), respectively; and Δ indicates the increment of each variable at each time step. Bond damping (i.e., η_n or η_s) is currently not considered in this formulation.

An added advantage of the bonded-sphere model is its capability of modeling particle breakage by allowing a bond to break, as demonstrated in [34]. As an example of a common bond breakage criterion, one can assume that a bond would break if the maximum normal or shear stress at the bond exceeds the corresponding normal or shear strength. In the linear parallel bond model, both the normal force and swinging moment contribute to the normal stress, while both the shear force and twisting moment contribute to the shear stress. In this study, particle breakage is not considered since the focus is on granular hopper flow. It is also noted that the bonded-particle approach can be applied to model very large particle deformation as well as conformal and non-conformal contact problems. For example, by using extremely fine spheres, this approach is capable of reproducing the scenario where a soft ball deforms into an approximate plane when hitting a rigid wall. However, there could be a numerical stability issue that, in the case of extremely high impacting velocity, the forefront spheres could penetrate into the inner layers of spheres, resulting in spurious sphere interactions. A careful consideration of the critical timestep is required to avoid such an issue. In addition, the particle deformation behavior could depend on the bond configuration, which may deviate from the continuum-based elastic deformation behavior. The situation could be worse in the case of large contact conformal deformation.

2.2. Intra- and inter-particle contacts

In the bonded-sphere DEM model, we distinguish two types of contacts. The first type of contact is termed the *intra-particle contact*, which refers to the contact between base spheres within the same multi-sphere particle. The second type is termed the *inter-particle contact*, which refers to the contact between spheres of different particles. For the intra-particle contact, its contact forces are calculated based on the linear parallel bond model described in Section 2.1. For the inter-particle contact, we adopt the Hertz-Mindlin contact model, which is a complete frictional contact model based on the Hertz theory [49] for contact normal forces and the Mindlin theory [50] for contact tangential forces. It takes into account the stiffness variation due to the change of contact areas during the collision of two elastic spheres. Normally, the Hertz-Mindlin contact model can be characterized by four parameters: Young's modulus E, Poisson's ratio ν, the coefficient of restitution e, and the coefficient of friction μ. The formulation of the Hertz-Mindlin contact model is presented in Section A, and the interested readers are referred to Mindlin [50], Di Renzo and Di Maio [51] for more details.

Once the contact models are chosen, a typical DEM computation cycle involves four key steps as shown in Fig. 2. For the first step, motions (e.g., positions and velocities) of all particles in the system at the current state are known and particle contacts are detected based on geometries and positions of all particles. Then, contact forces and moments are calculated based on the selected contact models and the contact features associated with each contact. In the third step, all external forces and moments experienced by a particle are summed and cast into the Newton–Euler equations to calculate the particle acceleration. Lastly, the velocity and position of each particle are obtained by integration of accelerations over time, where the second-order Velocity Verlet algorithm [52] is commonly adopted. The process is repeated for every particle in the system and for every time step, in which motions of and interactions between particles are fully resolved. Details of the governing equations and integration scheme are not presented in this work as they are well-established and can be found in DEM references such as [2,53,54].

3. Setup of the hopper flow test

In this section, we describe in detail the setup of the granular hopper flow test, including materials and calibrated DEM model parameters, the geometry of the hopper, the testing procedure, and methods for postprocessing. As for the DEM code, we use LIGGGHTS-INL, an open-source, capability-extended version of LIGGGHTS [55] that has been adopted in a number of recent DEM studies of deformable granular materials [56,57,33,34,58,59,35,32].

3.1. Materials and calibrated DEM model parameters

The materials being referenced in this work are the loblolly pine woodchips, which are commonly used as a biomass feedstock for conversion into biofuels or biochemicals. Fig. 3 shows a picture of the loblolly pine woodchips. While the woodchip samples considered in this work consist of various complex shapes, it is observed that these shapes can be grouped into two basic types, the fiber-shaped and the plate-shaped. Hence, in the DEM model, the fiber and plate templates are used to generate particles. As shown in Fig. 3, the fiber template is built from five non-overlapping spheres in one row, and the plate template is built from ten non-overlapping spheres in three rows. The base spheres have a radius of 1 mm and are bonded with their neighboring

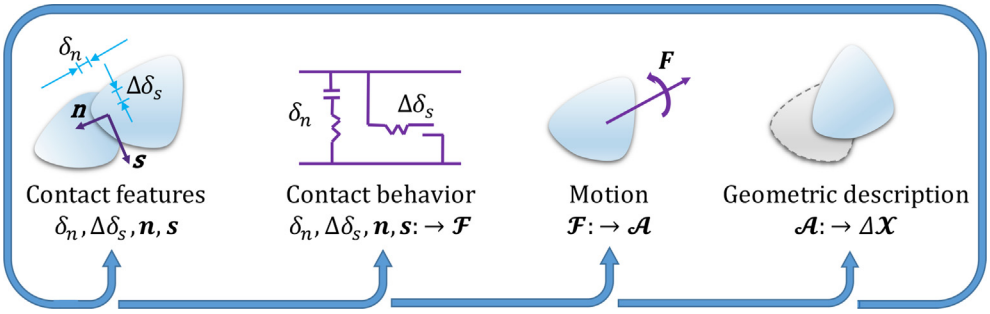

Fig. 2. The workflow and calculations of one typical DEM computational cycle. $\vec{\mathcal{F}}, \vec{\mathcal{A}}$ and $\vec{\mathcal{X}}$ indicate the general forces, accelerations, and positions of a particle. A generic contact model is shown in the workflow.

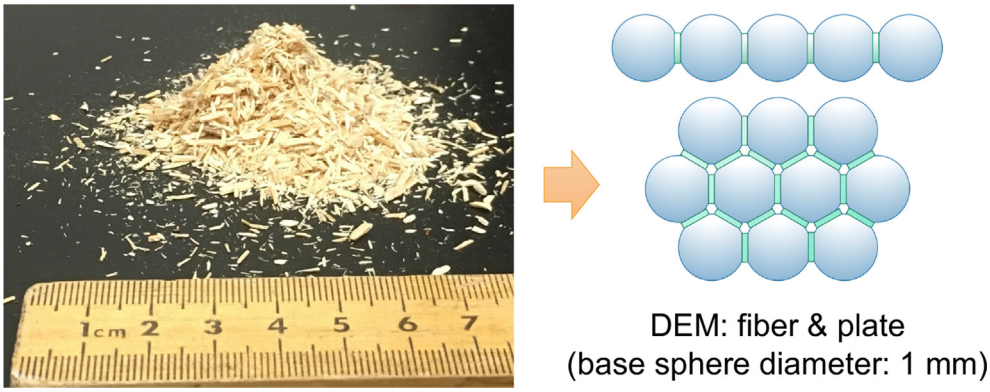

Fig. 3. Picture of the loblolly pine woodchips considered in this study and the two conceptualized shape templates for the bonded-sphere model.

spheres using the previously introduced bonded-sphere model. This conceptual simplification of shape templates greatly reduces the computational expenses while retaining the most prominent feature of particle shapes.

It is worth noting that if there is an overlap between two bonded base spheres, there will be a large repulsive force between these two base-spheres when the bond breaks. To prevent such an issue that could potentially cause DEM program errors, in LIGGGHTS, if a bond breaks and the base spheres overlap, the overlap will be set to zero so that no sudden repulsion takes place. This is handled internally by having an offset value that shrinks the overlap to zero once the base spheres start drifting apart. In addition, in cases where a base sphere is bonded with a specific set of neighboring base spheres, the sphere may experience significant displacement and make contact with another neighboring base sphere that is not initially bonded with it. Such cases may arise when a particle undergoes significant deformation. This issue could result in spurious particle behavior due to the additional intra-particle colliding interactions.

As most of the contact parameters in DEM are difficult, if not impossible, to be directly measured in experiments, a parameter calibration process is therefore needed. There are several excellent reviews in the literature discussing the procedures and challenges of calibrating contact parameters for a DEM model [60–62]. Usually, the calibration process aims to match benchmark metrics by varying contact parameters. In our recent publication [32], we have calibrated the contact parameters of the bonded-sphere DEM model using data from compression tests conducted on loblolly pine woodchips, and the calibrated DEM model parameters for woodchips are summarized in Table 1. Among these parameters, the particle density was measured from physical experiments, and the radii of base spheres and parallel bonds were determined based on the characteristic size of the woodchips being studied. The Poisson's ratio has a minimal influence on bulk behavior and a typical value for woodchips was set. A small coefficient of restitution was used considering the characteristics of woodchip particles. In addition, by envisioning a parallel bonded particle as a continuous elastic beam, the bond normal stiffness can be related to the material Young's modulus (E) and particle radius (R) [26], via $k_n^b = 2ER$. The calibration thus mainly focused on Young's modulus and contact friction. It was conducted through parametric studies of cyclic uniaxial loading tests that considered various values of Young's modulus and contact friction. The Young's modulus and contact friction were then determined by comparing the stress–strain histories between the laboratory experiments and the DEM simulations. It should be noted that both the Hertz-Mindlin contact model and the parallel bond contact model involve a stiffness parameter that characterizes the (hyper) elastic stage of the force–displacement contact behavior, and both stiffness parameters can be related to

Table 1
Calibrated model parameters of the woodchip samples (adopted from [32]).

Parameter	Symbol	Value	Unit
Density	ρ_s	430	kg/m^3
Sphere radius	R	0.5	mm
Young's modulus	E	10	MPa
Poisson's ratio	ν	0.3	-
Coefficient of restitution	e	0.1	-
Coefficient of friction	μ	0.5	-
Bond radius	R^b	0.5	mm
Bond normal stiffness	k_n^b	10	GN/m^3
Bond shear stiffness	k_s^b	0.6	GN/m^3
Wall Young's modulus	E_w	1.0	GPa
Wall friction coefficient	μ_w	0.5	-
Timestep	Δt	2.0	μs

the same Young's modulus (E), i.e., the continuum-sense Young's modulus of the material. The wall friction coefficient is set at 0.5, which higher than the value of 0.1 used in [32] to account for rougher wall materials used in the hopper flow test. The parameters summarized in Table 1 will be used in the subsequent hopper flow simulations.

3.2. Setup of the hopper flow tests

The sketch of the wedge-shaped hopper modeled in this study is shown in Fig. 4. In the corresponding DEM model, two surface meshes comprised of triangular elements are used to model the hopper walls. To minimize the computational cost, only a thin cross-section of the hopper is considered with a depth of $t_y = 0.01$ m in the y-direction, which is statistically sufficient compared with the particle size. A periodic boundary condition is prescribed for the domain boundaries in the y-direction. The initial particle packing is created following a rainfall method [63]. In particular, a given number (or mass) of particles are repeatedly inserted in a region above the hopper. The particles are then allowed to fall into the hopper under gravity. Once the hopper is filled up to a target height (0.18 m in this study), the particle insertion is stopped. Then, the particles in the hopper are allowed to settle until the packing reaches equilibrium. A criterion of equilibrium is to monitor whether the maximum sphere velocity among all the inserted particles has decreased below a threshold value (5 mm/s as specified in this study). Once the equilibrium is reached, extra particles that are above the target height are removed. Lastly, the particle packing is allowed to equilibrate again, in case that the action of particle removal induces disturbance to the packing.

For the discharging process, we follow a procedure similar to the hopper flow experiments reported in [36], which is designed to measure the critical arching width of biomass materials under self-weight and extra surcharge pressure. In this process, the hopper walls are first gradually raised along their tangential direction at a speed of 0.1 m/min. The size of the hopper orifice is thus gradually enlarged in time. The material critical arching width is then approximated as the minimum orifice size at which particles can continuously flow out of the hopper. As it will be presented later, most simulation scenarios yield a critical arching width smaller than 0.01 m. To facilitate a valid comparison of discharge rates at the steady state between different simulation scenarios, the movement of hopper walls will be stopped when the orifice size reaches 0.01 m in the simulation. The simulation is completed when all particles in the hopper are discharged or when clogging happens.

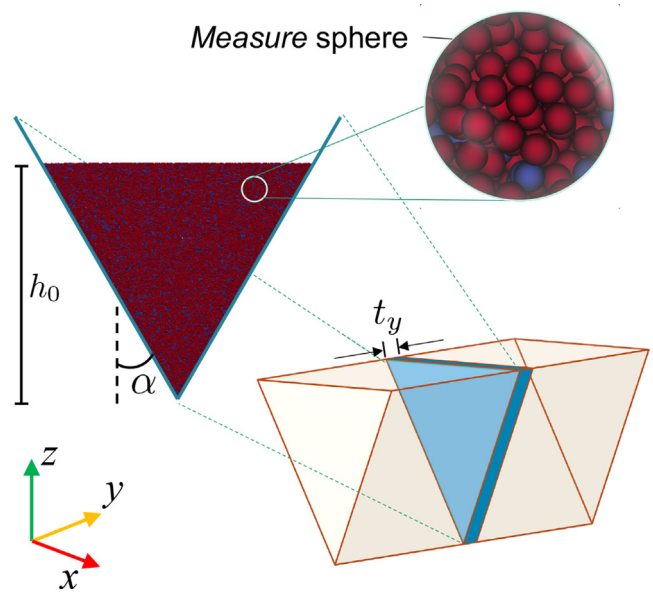

Fig. 4. Sketch of the wedge-shaped hopper. For the example problem considered in this work, the following specifications are used: h_0=0.18 m, α=30°, and t_y=0.01 m.

3.3. Simulation scenarios

To demonstrate the impact of particle deformation and shape irregularity on granular hopper flow, different simulation scenarios are designed as summarized in Table 2. The first three scenarios consider different types of particles: spherical particles, irregular-shaped rigid particles, and irregular-shaped deformable particles. The irregular-shaped rigid particles are modeled as clumps, i.e., collections of spheres with rigid connections [64]. They use the same fiber and plate templates as the irregular-shaped deformable particles (shown in Fig. 3) but do not consider particle-wise deformations. These three scenarios correspond to an increase in accuracy when representing particles in a DEM model, i.e., from basic spherical particles, to irregular particles, and to irregular-shaped deformable particles.

For deformable particles, their deformations are affected by not only the external loading but also their intrinsic properties (e.g., particle stiffness and particle shapes). For example, the fiber-shaped particles are easier to deflect than the plate-shaped particles when subject to the same external loading. To gain more insights into the particle deformability effects, two additional types of simulations are conducted. In the first type (scenarios E1 and E2 in Table 2), different particle Young's moduli are considered. In these scenarios, the bond normal and tangential stiffness are also scaled by the same factor when a different Young's modulus is used. In the second type (scenarios S-1, S-2, S-3, and S-4 in Table 2), different combinations (by mass ratio) of fiber-shaped and plate-shaped particles are considered. Moreover, as the fabric of initial particle packing may also affect the hopper flow behavior, each simulation scenario is repeated five times to account for the randomness in the initial particle generation process and to achieve statistically consistent results.

3.4. Calculation of field properties from DEM results

Continuum-sense field properties of the flow media, such as porosity and Cauchy stress, are not directly available from DEM results. In this study, a specific post-processing method is developed to calculate those properties. In particular, a *virtual measure sphere* is defined, with its center located at the position of interest and its

Table 2
Simulation scenarios considered in this study. E is the Young's modulus of a particle.

Scenarios	Description
I	Spherical particles of radius 0.5 mm, E=1e7 Pa
II	Irregular-shaped rigid particles, fiber 85%, plate 15%, E=1e7 Pa
III	Irregular-shaped deformable particles, fiber 85%, plate 15%, E=1e7 Pa
E-1	Irregular-shaped deformable particles, fiber 85%, plate 15%, E=1e6 Pa
E-2	Irregular-shaped deformable particles, fiber 85%, plate 15%, E=1e8 Pa
S-1	Irregular-shaped deformable particles, fiber 15%, plate 85%, E=1e7 Pa
S-2	Irregular-shaped deformable particles, fiber 30%, plate 70%, E=1e7 Pa
S-3	Irregular-shaped deformable particles, fiber 50%, plate 50%, E=1e7 Pa
S-4	Irregular-shaped deformable particles, fiber 70%, plate 30%, E=1e7 Pa

radius being ten times the radius of base spheres (as sketched in Fig. 4). The *measure* sphere would contain about 400∼600 base spheres, which are deemed to be sufficient for a representative elementary volume (REV) [8,65]. The field properties (e.g., the porosity or Cauchy stress) at the position of interest are then integrated from all spheres in the *measure* sphere (i.e., the REV). To evaluate the porosity, the solid volume fraction of the REV is first calculated as the volume of all base spheres in the REV divided by the volume of the REV. The porosity is then one minus the solid volume fraction. It should be pointed out that, in the current approach, the volume of contact overlapping is not excluded when calculating the solid volume of all base spheres. However, the volume of contact overlapping is negligible considering the low compressive pressure in the current hopper flow system. To evaluate the Cauchy stress, the virial stress of each base sphere is first computed in the DEM model. The Cauchy stress at a point is then calculated as the volume average of all virial stresses in the REV at that location. The formulation of virial stress is written as [66,40]

$$\vec{\sigma}_{ij} = \frac{1}{V_p} \Sigma_c F_i b_j \tag{5}$$

where Σ_c indicates the summation over all the contacts of a particle, V_p represents an individual sphere's occupied volume, F_i is the contact force, and b_j is the branch vector that connects the centroids of two particles. Particle stress is calculated using virial stress for both spherical and deformed particles. Fracture events are not considered, but the same approach can be used to calculate stress for fractured particles.

4. Results and discussions

In this section, we present results of the hopper flow simulations and discuss key observations. Specifically, we focus on the effects of irregular shapes and particle deformations on initial packing, flow characteristics, discharge rates, and stress fields. Classical solutions including Walker's theory and the extended Beverloo formula are also used to compare the stresses and discharge rates obtained from numerical simulations. Results of different shape combinations are briefly presented in the end to further explore the effects of irregular shapes on deformable particle flows.

4.1. Initial packing

We start this section by presenting the results of initial particle packing. Specifically, the initial porosity fields corresponding to simulation scenarios I (spherical), II (irregular-rigid), III (irregular-deformable, $E = 1e7$ Pa), E-1 (irregular-deformable, $E = 1e6$ Pa) and E-2 (irregular-deformable, $E = 1e8$ Pa) in Table 2 are reported. For these scenarios, the results of five realizations exhibited similar flow characteristics with no significant deviations. Thus, only one realization is used to prepare the following plots.

To begin with, Fig. 5 shows the porosity distributions of the initial particle packing for all five scenarios. It is observed that the packing of spherical particles exhibits the smallest porosity with a mean value around 0.4, which is very close to the statistical lower limit of 0.37 for a random packing with mono-sized, smooth and rigid spheres. The spatial distribution for spherical particle packing, as expected, is the most homogeneous among all five scenarios. By including shape irregularities (Fig. 5(b)), the packing porosity increases to over 0.6 and the spatial variations becomes more prominent. If particle deformation is further incorporated (Fig. 5(c)), the packing porosity is in-between those of spherical and irregular-rigid cases. By comparing irregular-shaped deformable particles with different stiffnesses (Fig. 5 general trend is observed, that as particle stiffness increases, the porosity of the initial packing increases. Spatial variations are also prominent in deformable particle packing.

As a more quantitative comparison, we also calculated the average porosity of the initial packing for all scenarios and present the results in Fig. 6. For deformable particles with different stiffnesses, their averaged initial packing porosity all falls between that of spherical particles and irregular-rigid particles. Moreover, as has been observed from the spatial distribution plots in Fig. 5, the porosity of deformable particles increases monotonically with particle stiffness. This can be explained by the fact that stiffer particles exhibit greater potentials to form stable arches, thus leading to more voids in the packing. As the particle stiffness increases to infinity, particles become rigid, while as stiffness decreases to zero, the bonded spheres behave as independent spheres without connecting bonds. Overall, irregular-shaped deformable particles can be regarded as an intermediate state between spherical particles and rigid particles.

4.2. Flow characteristics

For flow characteristics, we first focus on the flow patterns of different scenarios. The flow or discharge rate will be analyzed in the next section. From simulation results, it was observed that the hopper systems in scenarios I (spherical), III, E-1, and E-2 (irregular-deformable, $E = 1e6, 1e7$, and $1e8$), had continuous discharging until the hopper was completely empty. While in scenario II (irregular-rigid), flow did not occur, and particles stopped falling as soon as the hopper walls stopped moving (recall the testing procedure described Subsection 3.2: the hopper walls are first raised gradually, and then fixed when orifice width reaches 0.01 m).

To visualize the flow pattern, particles in the hopper are colored in layers. Snapshots of the hopper flow simulations during discharging are taken when the percent discharge reaches 30%, 50%, 70%, and 90%, as displayed in Fig. 7. Here, only flow patterns corresponding to scenario I and III are plotted, as scenario II (irregular-rigid) had clogging issue while scenarios E-1 and E-2 exhibited qualitatively similar flow patterns to scenario III.

Compared to scenario I where spherical particles are used, two main characteristics are observed in the flow of deformable particles. First, the top surface of the particle packing is concave, while it is a convex shape for spherical particle flows. In physical experiments of hopper flows, the concave-shaped top surface is the one commonly observed (e.g., grass seed [67]), matching observations made from the deformable particle flows. Second, the lateral shoulders of the top surface are not exactly leveled during the discharging, but rather seesawing downwards with one side lower than the other side alternately (e.g., the surface profiles at 70% and 90% discharge shown in Fig. 7(b)).

For the scenario of irregular-shaped rigid particles, we plot the settling of particles at clogging in Fig. 8(a). In this scenario, particles near the hopper orifice fell out due to the rise of the hopper walls. Once the hopper walls stopped moving, the remaining particles in the hopper stopped settling and formed a stable arch that can be visualized by the arch-shaped force chains shown in Fig. 8 (b). After that, no more particles could flow out due to the arching effects.

In the work of Walker [68], it was proposed that the critical arching width (i.e., the minimum orifice width for continuous particle flows) of a granular material is proportional to its shear strength. Since rigid particles cannot deform, they exhibit more sturdy interlocking behavior leading to a higher shear strength. Therefore, rigid particles have a higher critical arching width. This is consistent with simulations and observations from this study, i.e., rigid particles exhibit a larger critical arching width than deformable particles of the same shape. In other words, the potential

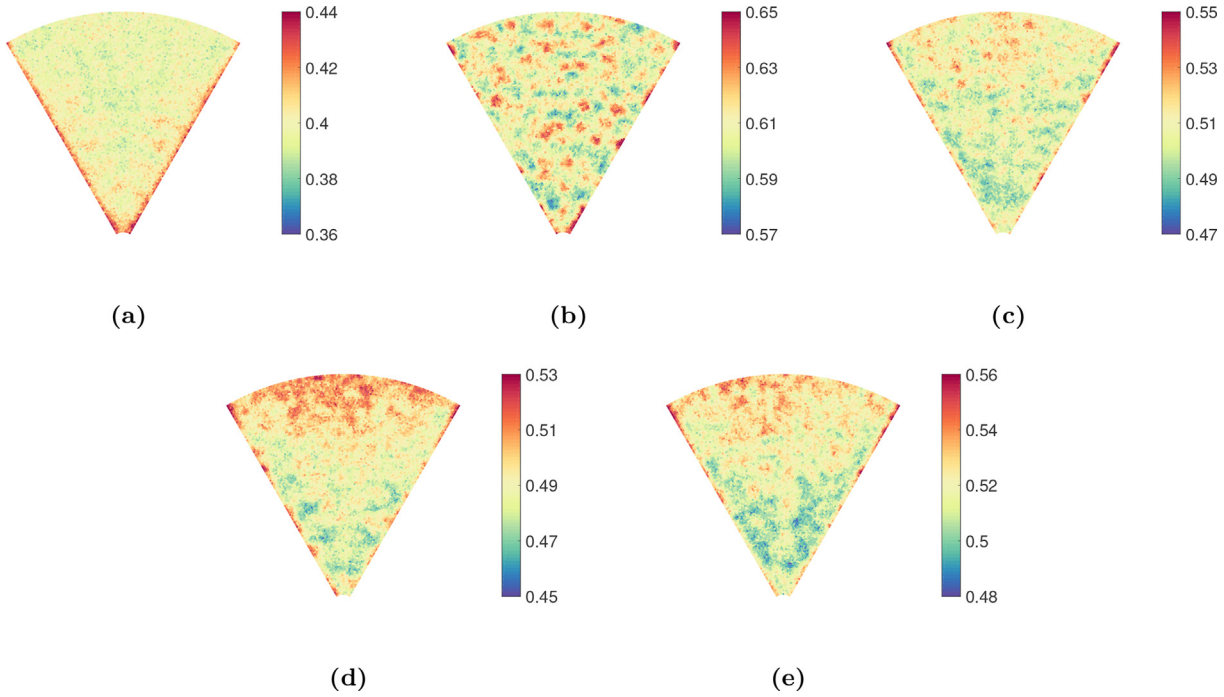

Fig. 5. Porosity distributions of the initial particle packing for simulation scenarios (a) I (spherical), (b) II (irregular-rigid), (c) III (irregular-deformable, $E = 1e7$ Pa), (d) E-1 (irregular-deformable, $E = 1e6$ Pa), (e) E-2 (irregular-deformable, $E = 1e8$ Pa).

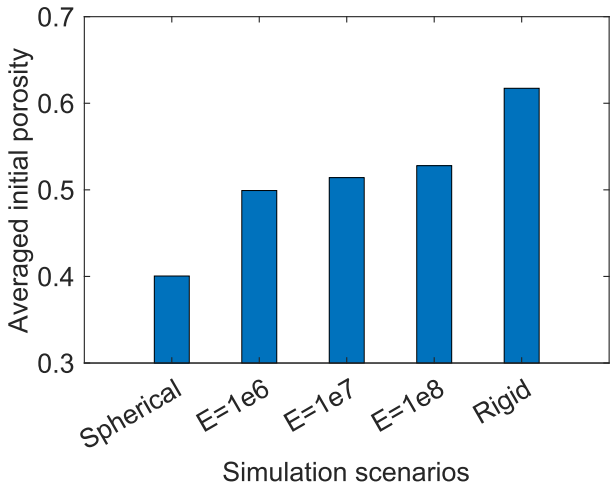

Fig. 6. The packing porosity of irregular-shaped deformable particles with different particle stiffnesses, compared to spherical particles and irregular-shaped rigid particles. The x-labels E = $1e6, 1e7$ or $1e8$ indicate Young's modulus.

of clogging for a granular material in hopper flow will be overestimated by a DEM simulation if particle deformations are not considered in the model.

4.3. Discharge rate

A quantitative comparison of discharge rates for all five scenarios (I, II, III, E-1, and E-2) is presented in Fig. 9. Five random realizations of the initial particle packing are generated for each scenario, corresponding to the five curves in each plot. It can be seen from Fig. 9 that the five random realizations yield consistent discharge rates, although the variation in the discharge rate increases slightly with increasing particle stiffness.

Among all five scenarios, spherical particles have the fastest discharge rate (100% discharge at 9.7 s shown in Fig. 9(a)). As mentioned before, clogging was observed in scenario II of rigid particle flows, which is reflected by the constant discharge percentage after approximately 7 s in Fig. 9(b). As for deformable particles (Fig. 9(c-e)), the plot shows that the time needed for a full discharge increases as the particle stiffness increases. Specifically, the time for a full discharge corresponding to $E = 1e6, 1e7$, and $1e8$ Pa is 23.6 (0.63), 25.6 (0.81), and 27.3 (1.31) seconds, respectively. The number in the bracket is the standard deviation calculated based on the five random realizations. A regression analysis yields the following simple relationship between the time t for a full discharge and the particle stiffness E

$$t = 0.8034 \ln(E) + 12.55 \tag{6}$$

The coefficient of determination $R^2 = 0.9978$ for the above relationship. An extreme case of this trend is the rigid particle flows, where an infinite stiffness corresponds to an infinite discharge time, i.e., clogging. These findings show that the discharge rate of granular hopper flow is negatively correlated to the particle stiffness for irregular-shaped deformable particles.

4.4. Particle and wall stresses

Particle and wall stresses in granular hopper flow are important metrics for the design of hopper geometry and operation conditions. Fig. 10 shows distributions of vertical and horizontal particle stresses at 60% discharge for deformable particle flows with different particle stiffnesses (scenarios III, E-1, and E-2). Though some subtle differences can be observed, the stress fields appear qualitatively similar. Particles near the hopper center line, where most of the flow occurs, are subject to horizontal stresses that are much larger than their vertical counterparts. The contours of horizontal stress present arch-like profiles, which become more prominent as the particle stiffness increases. Such prominent arch-like profiles may lead to a slower discharge rate and even clogging (e.g.,

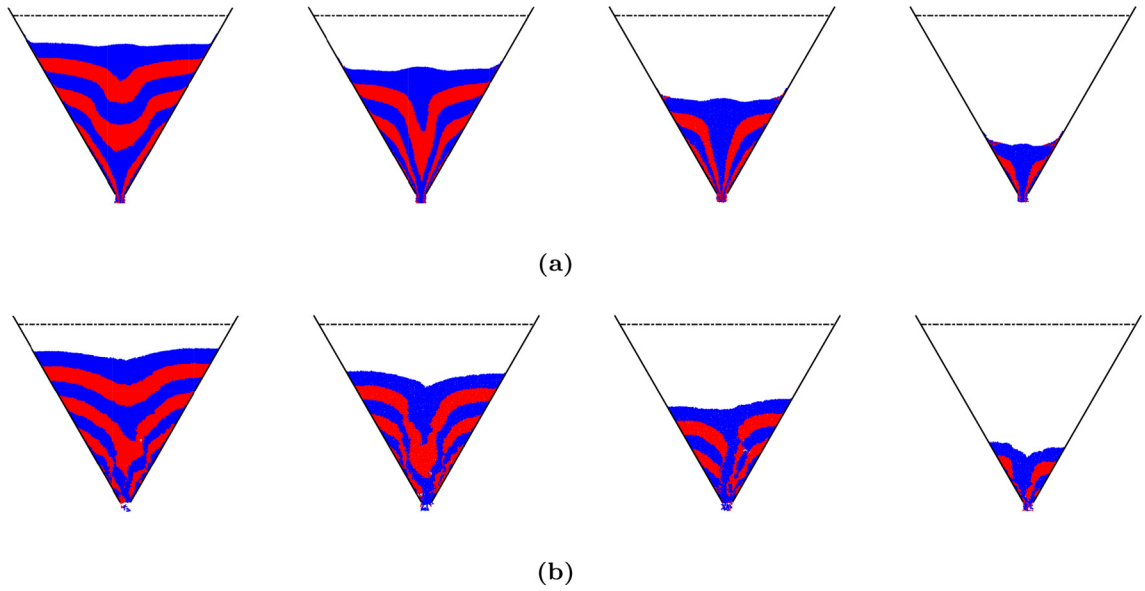

Fig. 7. Snapshots showcasing the flow patterns when the percent discharge is at 30%, 50%, 70%, and 90%: (a) spherical particles, (b) irregular-shaped deformable particles.

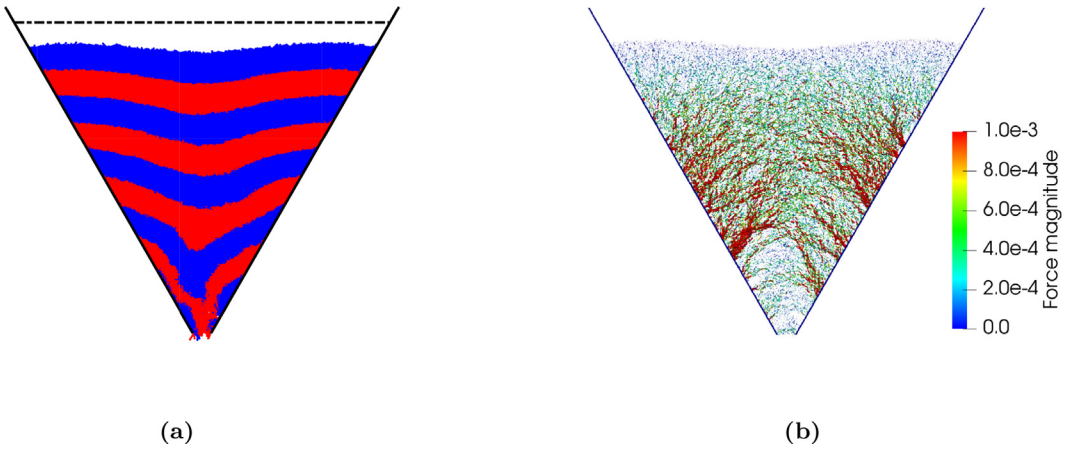

Fig. 8. The settling pattern (a) and force chains (b) in the hopper flow with irregular-shaped rigid particles, at t = 10 s after the stable clogging issue happened. (Unit of force: N).

the arch-like profile observed in the clogged rigid particle flows Fig. 8(b)). Particles in the orifice vicinity experience low stress because the converging hopper walls support the material above. In addition, the vertical stress profiles also present significant fluctuations with a clear zonal-like pattern, as can be observed in Fig. 9 (e). The same type of spatial fluctuations was also observed in the bulk density field in physical experiments of sand flow [69] and in stress fields in 2D DEM simulations of irregular-rigid particle flows [8]. In explaining this phenomenon, Baxter et al. [69] has proposed a theory of decompression waves propagating upwards at a much higher speed than the flow itself.

To gain insights into the stresses experienced by the hopper wall, we probe the normal and shear stresses of the hopper wall at a point located 0.035 m above the orifice for scenario III (deformable particles, $E = 1e7$ Pa) and plot them in Fig. 11(a). While the normal and shear stresses fluctuate over time, their averaged values over time (e.g., after 10 s) are asymptotically stable, which indicates an approximately steady discharge. In order to trace the correlation between the normal and shear stresses, the mobilized wall friction, defined as the ratio of shear stress to normal stress, is plotted in Fig. 11(b). The average mobilized wall friction over time is around 0.47, which is very close to the specified wall friction coefficient of 0.5. As a comparison, the average mobilized wall friction obtained from spherical particle flow is only about 0.29, which means that about 40% of the wall friction cannot be mobilized without the consideration of irregular particle shapes. A relevant finding was reported in a previous study, where it was shown that particle shape effect accounts for approximately 40% of the shear resistance of a granular material [22].

4.5. Comparison with classical solutions

To demonstrate the reliability of the present DEM model, in this section, we compare stresses and discharge rates from DEM simulations with their corresponding analytical or empirical solutions available in the literature. Specifically, the analytical solution by Walker [68] for predicting the vertical stress of particles at the hopper center and the normal stress on the hopper wall and the extended Beverloo formula [70] for predicting discharge rate are adopted. The extended Beverloo formula is a modification of the original Beverloo law [71] to suit wedge-shaped hoppers with a

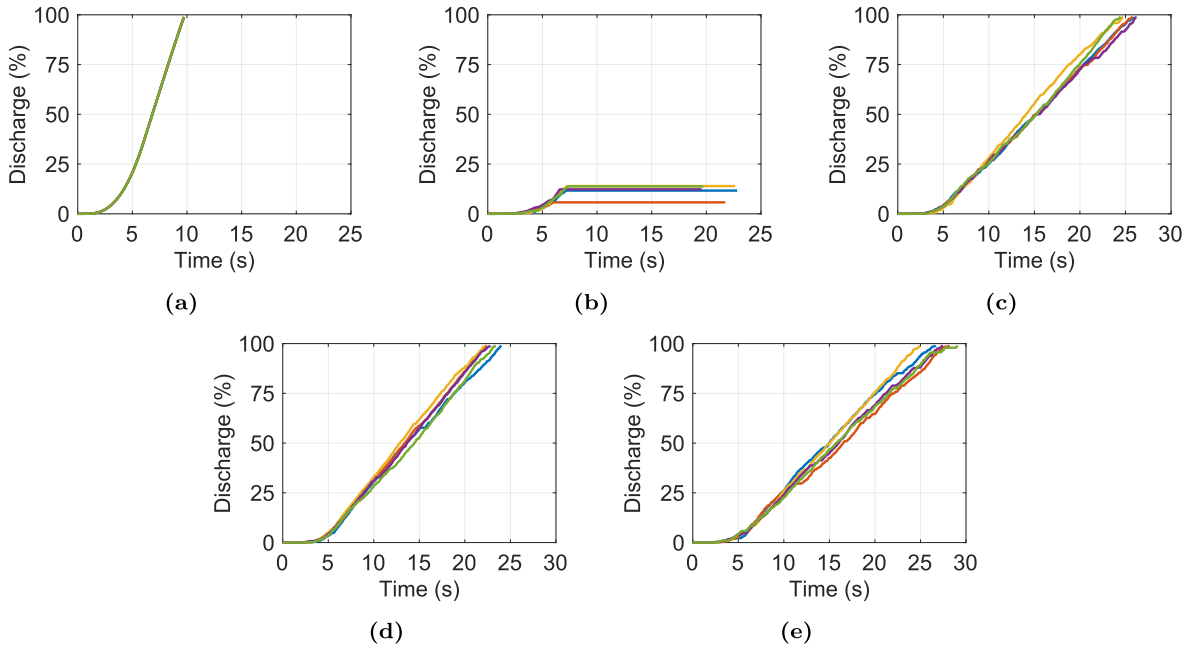

Fig. 9. Percentage of discharged particles vs. time for simulation scenarios: (a) I (spherical), (b) II (irregular-rigid), (c) III (irregular-deformable, $E = 1e7$ Pa), (d) E-1 (irregular-deformable, $E = 1e6$ Pa), (e) E-2 (irregular-deformable, $E = 1e8$ Pa). For each scenario, the five curves correspond to five random realizations of initial packing.

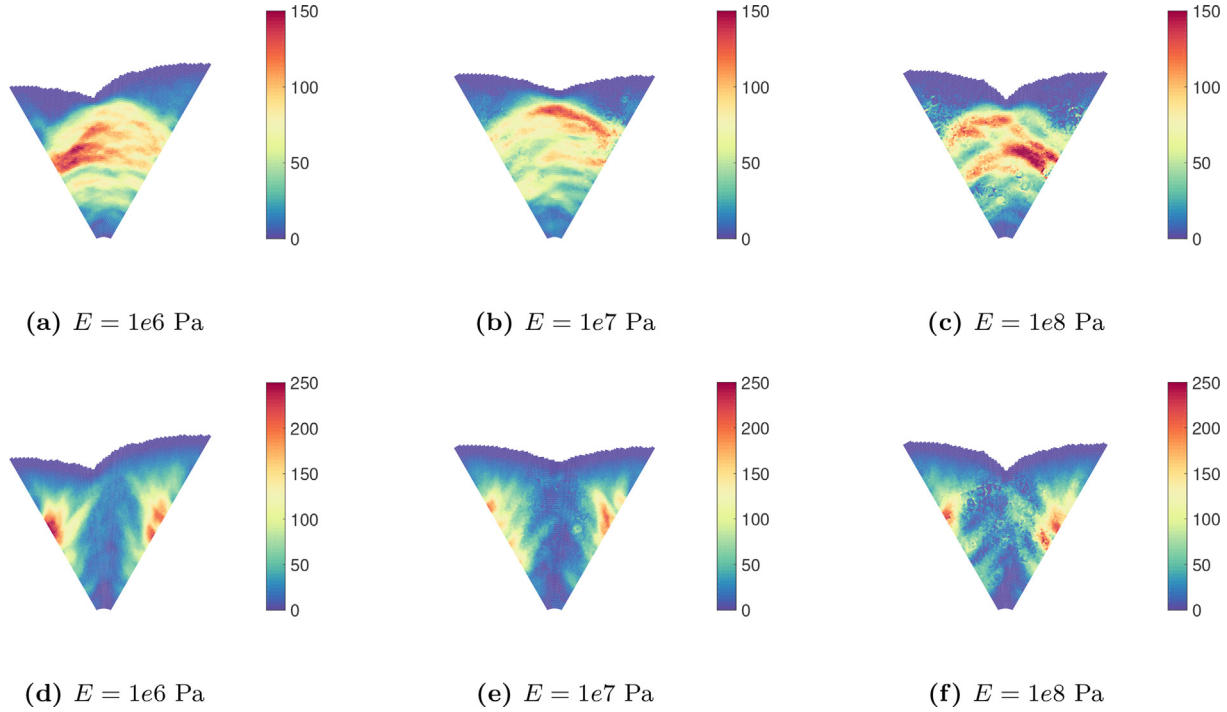

Fig. 10. Distributions of horizontal (top row) and vertical (bottom row) particle stresses (unit: Pa) at 60% discharge for deformable particle flows with different particle stiffnesses.

non-circular orifice. Formulations of these two classical solutions are briefly presented in Appendices B and C.

Table 3 summarizes the parameters of Walker's solution and the extended Beverloo formula that will be used in later calculations. In this table, the bulk friction angle ϕ of the particles is obtained from additional angle of repose tests. The wall friction angle ϕ_w is estimated from the mobilized wall friction in the hopper flow simulations. The stagnant angle ϕ_d is assumed to have the same value as the wall friction angle. Parameters C and λ for the extended Beverloo formula are determined based on their empirical values as well as the simulation fittings. Detailed descriptions of these parameters are included in Appendices B and C.

Fig. 12 shows the comparison of DEM simulations with Walker's solution for scenario I (spherical). The stresses are calculated at the time when the hopper walls start to rise up. At this time, the stress state transitions from active to passive in which Walker's theory

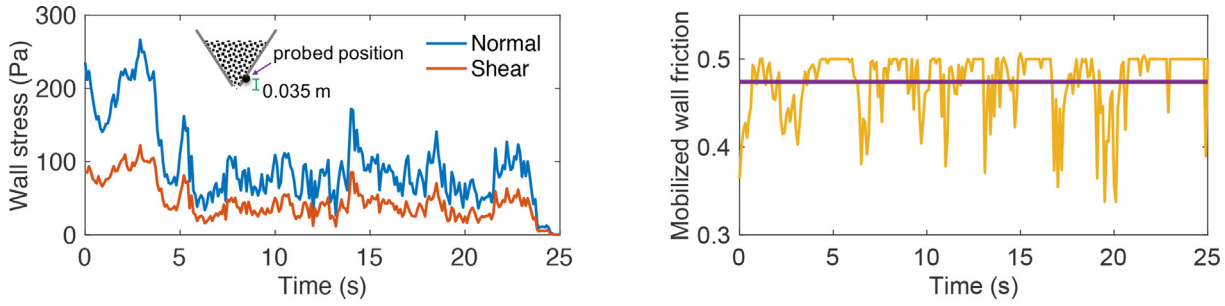

(a) Normal and shear stresses (b) Mobilized wall friction

Fig. 11. Results of (a) the normal and shear stresses of the hopper wall, and (b) the mobilized wall friction over the entire simulation for scenario III (irregular-deformable, $E = 1e7$). The solid line in (b) is the average mobilized wall friction.

Table 3
Parameters of Walker's solution (Eq. 22) and and the extended Beverloo formula (Eq. 28).

	h_0 (m)	ρ_b (kg/m^3)	α	ϕ	ϕ_w	D	C	λ	ϕ_d
Spherical	0.18	258	30°	18°	16°	1	0.62	1.5	16°
Irregular-shaped deformable	0.18	209	30°	42°	26°	1	0.58	3.7	42°

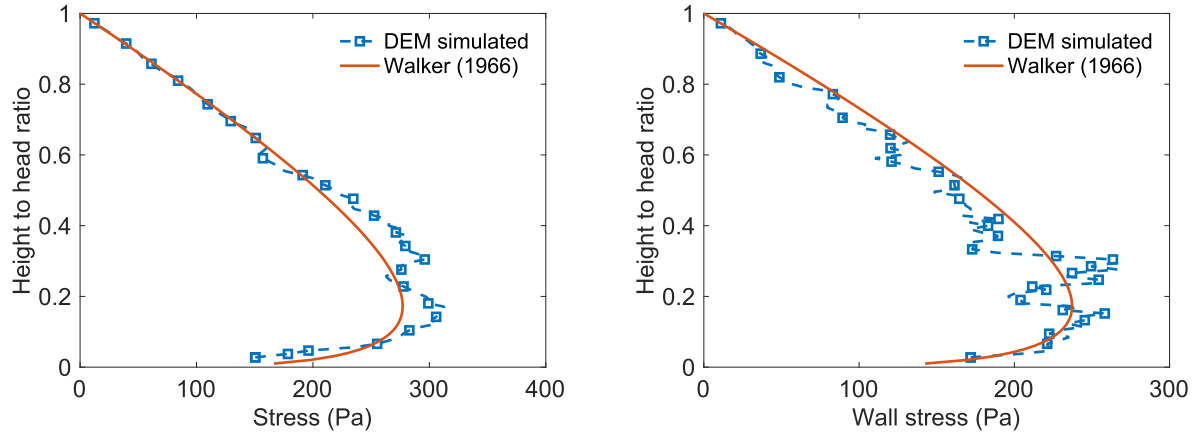

(a) Vertical stress of particles (b) Normal stress along the wall

Fig. 12. Comparison of DEM simulations with Walker's theory for scenario I (spherical): (a) vertical stress of particles along the hopper center line, and (b) the normal stress of the right hopper wall.

applies. As can be observed, the particle stress and wall stress present similar profiles with a clear trend of increasing and then decreasing from top to bottom. There are slight fluctuations in the stress profiles of DEM simulations, but not in Walker's solution. Such fluctuations are not numerical artifacts but are due to the discrete nature and dynamic responses of granular hopper flow [14,8]. Overall, both the simulated particle stress and wall stress exhibit good agreements with the corresponding Walker's solution.

The particle stress and wall stress for scenario III (irregular-deformable) are shown in Fig. 13. Similar to scenario I (spherical), both particle and wall stress profiles for irregular-shaped deformable particles present an increasing and then decreasing trend from top to bottom. However, near the orifice (height-to–head ratio of 0.2–0.4), the particle and wall stresses from DEM simulations are slightly higher than the counterparts by Walker's solution. A possible reason may lie in the hopper filling process, where particles are rain-falling into the hopper from a certain height. The particle kinetic energy would prestress the particles when they collide with each other or the hopper walls, and the prestress remains as a fact of particle interlocking. In addition to the hydrostatic pressure due to self-weight, the prestress due to collision and interlocking makes the particles exhibit higher stresses than the analytical results predicted by Walker's solution. This phenomenon could be even severer for irregular-shaped deformable particles as they exhibit stronger particle interlocking than spherical particles. Nevertheless, the simulated particle stress and wall stress exhibit a reasonable consistent trend with Walker's solution. The results suggest that, for scenarios considered in this study, the particle stress or wall stress in the granular hopper flow with irregular-shaped deformable particles have matched and can be approximated by Walker's theory.

The comparison of discharge rates obtained from DEM simulations and the extended Beverloo formula is presented in Fig. 14. During the first 6 s when the hopper walls are rising up, the discharge rate keeps increasing due to the increasing orifice size. After the hopper walls stop moving, discharge rate remains statistically constant most of the time, except for the short period near the end of the discharge process. For both scenarios I (spherical) and III (irregular-deformable), the simulated discharge rate matches very well with the empirical results predicted by the extended Beverloo

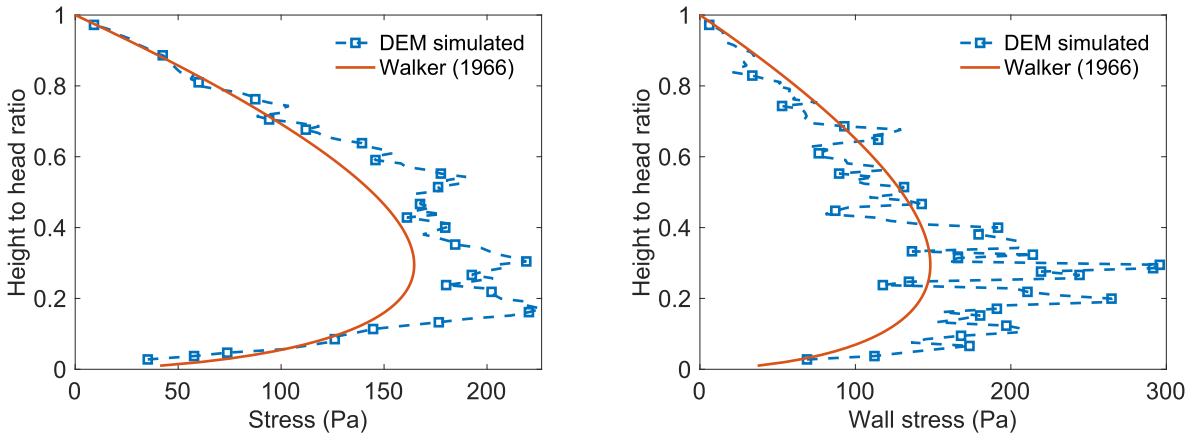

(a) Vertical stress of particles (b) Normal stress along the wall

Fig. 13. Comparison of DEM simulations with Walker's theory for scenario III (irregular-deformable): (a) vertical stress of particles along the hopper center line, and (b) the normal stress of the right hopper wall.

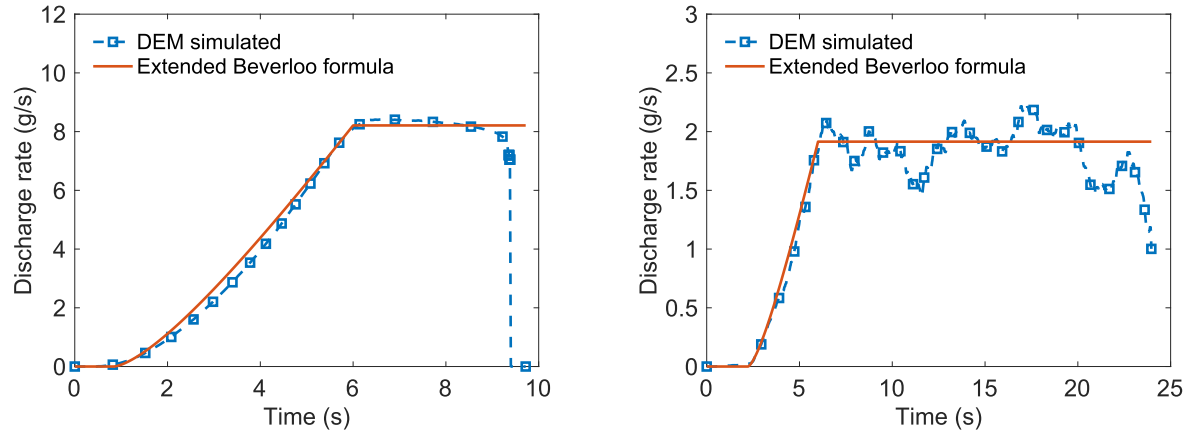

(a) Spherical particles (b) Irregular-shaped deformable particles

Fig. 14. The discharge rate from DEM simulations and the extended Beverloo formula for (a) scenario I (spherical), and (b) scenario III (irregular-deformable).

formula. It should be pointed out that although the Beverloo's parameters C and λ are fitted from DEM simulations, they are consistent with the suggested values reported in [71,70]. By comparing the values of C and λ for irregular-shaped deformable particles and spherical particles, we can identify the effects of shape irregularity on the discharge rate from two aspects. First, the shape irregularity would result in a higher bulk void fraction, leading to larger values of parameter C. Second, it increases the empty annulus effect [70, p. 295] and thus leads to larger values of parameter λ. A quantitative correlation between shape irregularity and the Beverloo's parameters would be of great value to industrial hopper design and merits more detailed studies in the future.

4.6. Effects of particle shape combinations

Lastly, we present the results of different shape combinations (scenarios III, S-1, S-2, S-3, and S-4 in Table 2) to further explore the effects of particle shapes on irregular-shaped deformable particle flows. For brevity, only results of the averaged initial packing porosity and discharge profiles are presented.

Fig. 15 plots the averaged initial packing porosity for irregular-shaped deformable particles with different shape combinations. It

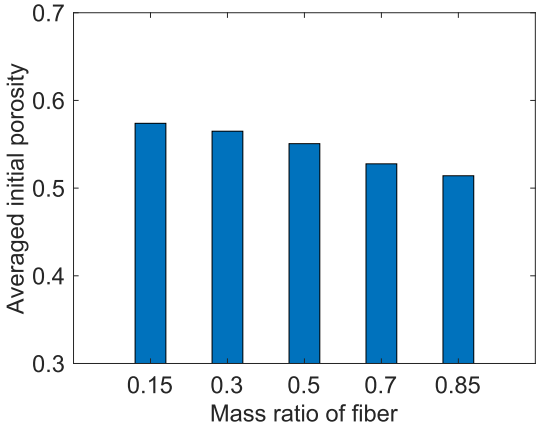

Fig. 15. The packing porosity of irregular-shaped deformable particles with different fractions of fiber-shaped and plate-shapes particles.

can be seen that the packing porosity decreases as the fraction of fiber-shaped particles increases. This phenomenon can be explained by differences of the two particle templates' resistance to

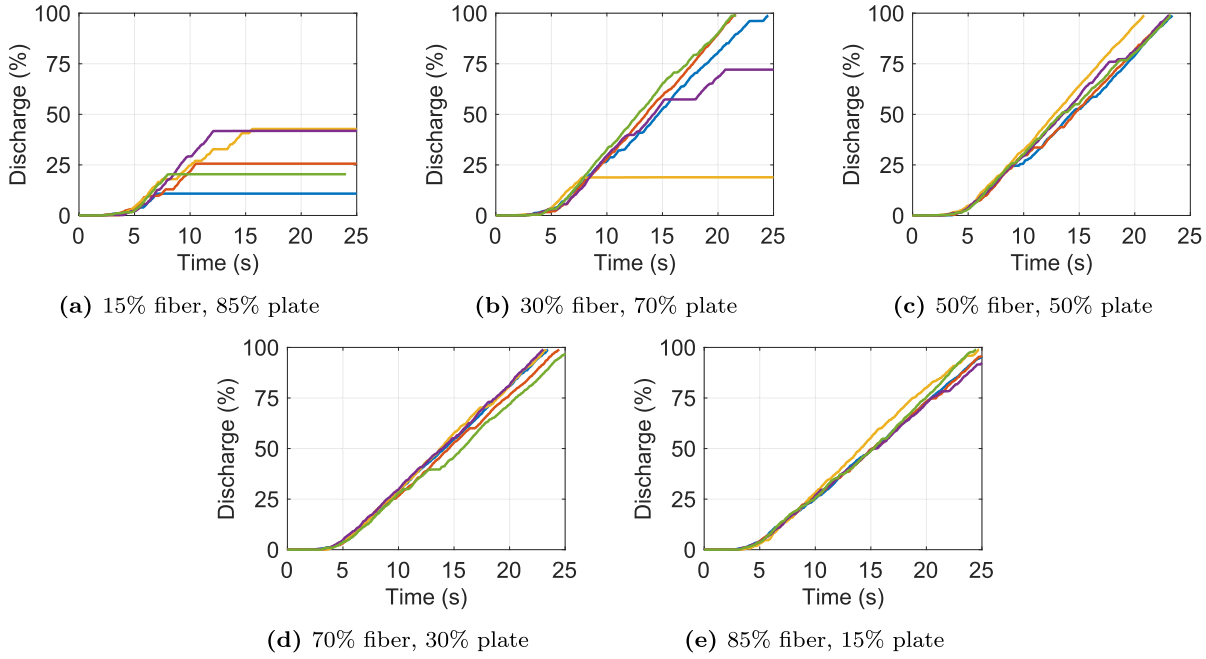

Fig. 16. Percentage of discharged particles vs. time for simulation scenarios: (a-d) S-1, S-2, S-3, and S-4 (irregular-deformable, fiber = 15%, 30%, 50%, and 70%, respectively), (e) III (irregular-deformable, fiber = 85%). For each scenario, the five curves correspond to five random realizations of initial packing.

bending. Compared to plate-shaped particles, fiber-shaped particles have a lower moment of inertia, and thus have less resistance to bending and are more deformable to pack in tighter (i.e., smaller porosity). In addition, particle geometry is also a factor through available degrees of freedom. The rotational symmetry about their axis also allows the fiber-shaped particles to pack tighter.

The discharge profiles for irregular-shaped deformable particles with different shape combinations are shown in Fig. 16. The trend of shape combination effects on the discharge profile changes, depending on whether the fiber-shaped particles or the plate-shaped particles dominate. As plots Fig. 16(a-c) show, when the plate-shaped particles dominate, more plate-shaped particles lead to an increased tendency of clogging. This phenomenon can be partially interpreted by the fact that the plate-shaped particles have a larger geometric size than the fiber-shaped particles. This means that plate-shaped particles require a larger orifice size to maintain a continuous outflow. Interestingly, as the ratio of fiber-shaped particles increases above 50%, the discharge rate gradually decreases (see Fig. 16(c-e)). The time for a full discharge corresponding to the fiber ratio of 50%, 70%, and 85% is 22.8 (1.07), 23.9 (0.97), and 25.7 (0.81) seconds, respectively. The number in the bracket is the standard deviation calculated based on five random realizations. Compared to plates, the fiber-shaped particles have a larger aspect ratio, which may increase particle interlocking that hinders discharge. When the percentage of fibers is greater than 50%, such increased particle interlocking potentials may offset the effects of plate-shaped particles' larger geometric sizes. The observations made from these simulations shed light on the effects of different particle shape combinations on granular hopper flow and motivate future studies on shape effects in deformable particle flows.

5. Conclusions

We have presented a bonded-sphere discrete element model to simulate and study the flow behavior of irregular-shaped deformable particles in a wedge-shaped hopper. In this model, a cluster of bonded-spheres is employed to simultaneously capture irregular particle shapes and particle-wise deformations via inter-particle bonds. Model parameters are calibrated using experimental data of loblolly pine woodchips. To better understand the effects of irregular shapes, and more importantly, particle deformations on behavior of granular hopper flows, we have set up simulation models with spherical, irregular-shaped rigid, and irregular-shaped deformable particles and performed detailed quantitative analysis of hopper flows. Key findings of this study are summarized below.

1. The increase of particle stiffness increases the packing porosity and the packing porosity of irregular-shaped deformable particles falls within that of spherical and irregular-shaped rigid particles.
2. The increase of particle stiffness decreases the flow rate in the hopper. Rigid particles tend to have clogging issues whereas deformable particles have less chance to, indicating particle deformation reduces the critical bridging width in the hopper flow.
3. The particle and wall stresses in irregular-shaped deformable particle flows exhibit significant temporal and spatial fluctuations, but the general trends agree well with Walker's solution. Irregular shapes increase the mobilized wall friction by about 40% compared to spherical particles.
4. Discharge rates of hopper flow can be well fitted by the extended Beverloo formula. However, the correlation between Beverloo's parameters and shape irregularity and particle stiffness merits further studies.
5. Fiber- and plate-shaped particles have competing effects on discharge rates. When the mass ratio of fiber-shaped particles is less than 50%, the discharge rate increases with the fiber percentage. The trend reverses when the fiber-shaped particles are more than 50%. The porosity, on the other hand, decreases monotonically with increasing fiber-shaped particles.

Using the model developed in this study, future work will investigate a wider range of particle sizes, shapes, stiffnesses, and hopper geometries and will approach quantitative relationships between particle characteristics and hopper flow behavior.

Declaration of Competing Interest

The authors declare that they have no known competing financial interests or personal relationships that could have appeared to influence the work reported in this paper.

Acknowledgments

This work is mainly supported from U.S. Department of Energy's Bioenergy Technologies Office (BETO) Feedstock-Conversion Interface Consortium (FCIC), under DOE Idaho Operations Office with Contract No. DE-AC07-05ID14517. This work also receives partial support from the U.S. Department of Energy's Office of Energy Efficiency and Renewable Energy (EERE) under the BETO with Award No. DE-EE0008255. The research used resources in the High Performance Computing Center at INL, which is supported by the Office of Nuclear Energy of the U.S. Department of Energy and the Nuclear Science User Facilities under Contract No. DE-AC07-05ID14517. The lead author performed the research when being solely affiliated with Clemson University and being an academic visitor at Idaho National Laboratory previously. The authors also appreciate the comments and discussions from Drs. J.L. Klinger and T.L. Westover at Idaho National Laboratory.

Appendix A. Hertz-Mindlin contact model

In the Hertz-Mindlin contact model [49–51], the contact force is evaluated as

$$\vec{F} = k_n \delta_n \vec{n} - \gamma_n \vec{v}\vec{n} + k_t \delta_t \vec{t} - \gamma_t \vec{v}\vec{t} \tag{7}$$

where δ_n and δ_t are the normal overlap and relative tangential displacement, respectively; $\vec{v}$ is the particle relative velocity; and $\vec{n}$ and $\vec{t}$ are the normal and tangential directions, respectively; k_n, k_t, γ_n, and γ_t are the normal stiffness, tangential stiffness, normal and tangential viscoelastic damping constants, respectively, and is calculated as

$$k_n = \frac{4}{3} E^* \sqrt{R^* \delta_n} \tag{8}$$

$$k_t = 8 G^* \sqrt{R^* \delta_n} \tag{9}$$

$$\gamma_n = -2\sqrt{\frac{5}{6}} \beta \sqrt{S_n m^*} \tag{10}$$

$$\gamma_t = -2\sqrt{\frac{5}{6}} \beta \sqrt{S_t m^*} \tag{11}$$

$$S_n = 2E^* \sqrt{R^* \delta_n} \tag{12}$$

$$S_t = 8G^* \sqrt{R^* \delta_n} \tag{13}$$

$$\beta = \frac{\ln(e)}{\sqrt{\ln^2(e) + \pi^2}} \tag{14}$$

with E^*, G^*, R^*, and m^* indicating the equivalent Young's modulus, shear modulus, particle size, and particle mass, respectively, which are calculated as

$$\frac{1}{E^*} = \frac{1 - v_1^2}{E_1} + \frac{1 - v_2^2}{E_2} \tag{15}$$

$$\frac{1}{G^*} = \frac{2(2 - v_1)(1 + v_1)}{E_1} + \frac{2(2 - v_2)(1 + v_2)}{E_2} \tag{16}$$

$$\frac{1}{R^*} = \frac{1}{R_1} + \frac{1}{R_2} \tag{17}$$

$$\frac{1}{m^*} = \frac{1}{m_1} + \frac{1}{m_2} \tag{18}$$

where the subscripts 1 and 2 indicate particles, and v is the Poisson's ratio.

Appendix B. Particle and wall stress: Walker's theory

To calculate the particle stress or wall stress during discharging, Walker [68] developed an analytic solution based on the slice element method. In this solution, the average vertical stress $\bar{\sigma}_v$ of the particles, and the normal stress σ_n of the hopper wall at any height h, can be calculated as

$$\bar{\sigma}_v = \frac{\rho_b g h}{\xi - 1} \left[1 - \left(\frac{h}{h_0} \right)^{\xi - 1} \right] \tag{19}$$

$$\sigma_n = D \bar{\sigma}_v \frac{1 + \sin\phi \cos 2\beta}{1 - \sin\phi \cos 2(\alpha + \beta)} \tag{20}$$

in which

$$\beta = \frac{1}{2} \left[\phi_w + \arcsin\left(\frac{\sin\phi_w}{\sin\phi} \right) \right] \tag{21}$$

$$\xi = \frac{D \sin\phi \sin 2(\alpha + \beta)}{\tan\alpha [1 - \sin\phi \cos 2(\alpha + \beta)]} \tag{22}$$

where h_0 is the initial filled height; ρ_b is the bulk density; g is the acceleration; α is the hopper half-angle; ϕ is the angle of internal friction of the bulk material; ϕ_w is the angle of internal friction between the bulk material and the hopper; D is the stress distribution factor, taken as unity for simplicity [68].

Appendix C. Discharge rate: the extended Beverloo formula

Based on the results of hopper flow experiments with a variety of materials and hopper geometries, Beverloo et al. [71] proposed an empirical formula predicting the discharge rate W_B of granular hopper flow

$$W_B = C \rho_b \sqrt{g} (D_0 - \lambda d)^{2.5} \tag{23}$$

where C is a unit-less coefficient that depends on the particle friction and wall friction; D_0 is the diameter of the orifice; λ is a shape factor accounting for the particle shape effects; d is the particle diameter. The friction-related parameter C normally takes a value in the range from 0.58 (for high-friction particles) to 0.64 (for exceptionally smooth particles) [70]. The shape factor λ is about 1.4 for spherical particles and may take larger values for angular particles (e.g., 2.9 for sand) [71,70].

The Beverloo formula can be applied to non-circular orifices, such as square, rectangle or triangle, by taking the modified proposed by Nedderman [70]

$$W_B = \frac{4C}{\pi} \rho_b A' \sqrt{g D_h'} \tag{24}$$

where A' and D_h' are the effective area and the effective hydraulic diameter of the orifice after the removal of the empty annulus. As an example, for a $b \times l$ rectangle orifice, A' and D_h' are calculated as

$$A' = (b - \lambda d)(l - \lambda d) \tag{25}$$

$$D_h' = \frac{A'}{(b + l - 2\lambda d)/2} \tag{26}$$

As pointed out by Nedderman [70], the Beverloo formula is only applicable to bunkers or hoppers with a funnel flow behavior. In the case of mass flow, the effect of the hopper half-angle α becomes important. Thus, Nedderman [70] proposed to extend the Beverloo formula with a mass flow coefficient $F(\alpha, \phi_d)$, such that

$$W = W_B F(\alpha, \phi_d) \tag{27}$$

in which

$$F(\alpha,\phi_d)=\begin{cases}(\tan\alpha\tan\phi_d)^{-0.35}, & \text{if}\,\alpha<90^\circ-\phi_d\\ 1, & \text{otherwise}\end{cases} \quad (28)$$

where W is the modified outflow rate; ϕ_d is the angle between the stagnant zone boundary and the horizontal. The condition $\alpha<90^\circ-\phi_d$ can be regarded as a mass flow criterion.

References

[1] J. Horabik, M. Molenda, Mechanical properties of granular materials and their impact on load distribution in silo: a review, Scientia Agric. Bohem. 45 (4) (2014) 203–211.
[2] P. Cundall, O. Strack, A discrete numerical model for granular assemblies, Géotechnique 29 (1) (1979) 47–65.
[3] S. Masson, J. Martinez, Effect of particle mechanical properties on silo flow and stresses from distinct element simulations, Powder Technol. 109 (1–3) (2000) 164–178.
[4] T. Goda, F. Ebert, Three-dimensional discrete element simulations in hoppers and silos, Powder Technol. 158 (1–3) (2005) 58–68.
[5] W. Ketterhagen, J. Curtis, C. Wassgren, B. Hancock, Predicting the flow mode from hoppers using the discrete element method, Powder Technol. 195 (1) (2009) 1–10.
[6] Y. Zhang, F. Jia, Y. Zeng, Y. Han, Y. Xiao, DEM study in the critical height of flow mechanism transition in a conical silo, Powder Technol. 331 (2018) 98–106.
[7] H. Zhu, A. Yu, Y. Wu, Numerical investigation of steady and unsteady state hopper flows, Powder Technol. 170 (3) (2006) 125–134.
[8] G. Mollon, J. Zhao, Characterization of fluctuations in granular hopper flow, Granular Matter 15 (6) (2013) 827–840.
[9] R. Kobyłka, J. Horabik, M. Molenda, Numerical simulation of the dynamic response due to discharge initiation of the grain silo, Int. J. Solids Struct. 106 (2017) 27–37.
[10] W. Ketterhagen, J. Curtis, C. Wassgren, B. Hancock, Modeling granular segregation in flow from quasi-three-dimensional, wedge-shaped hoppers, Powder Technol. 179 (3) (2008) 126–143.
[11] Y. Yu, H. Saxén, Segregation behavior of particles in a top hopper of a blast furnace, Powder Technol. 262 (2014) 233–241.
[12] R. Balevičius, R. Kačianauskas, Z. Mroz, I. Sielamowicz, Analysis and DEM simulation of granular material flow patterns in hopper models of different shapes, Adv. Powder Technol. 22 (2) (2011) 226–235.
[13] J. Wan, F. Wang, G. Yang, S. Zhang, M. Wang, P. Lin, L. Yang, The influence of orifice shape on the flow rate: A DEM and experimental research in 3D hopper granular flows, Powder Technol. 335 (2018) 147–155.
[14] P. Cleary, M. Sawley, DEM modelling of industrial granular flows: 3D case studies and the effect of particle shape on hopper discharge, Appl. Math. Model. 26 (2) (2002) 89–111.
[15] R. Balevičius, R. Kačianauskas, Z. Mróz, I. Sielamowicz, Discrete-particle investigation of friction effect in filling and unsteady/steady discharge in three-dimensional wedge-shaped hopper, Powder Technol. 187 (2) (2008) 159–174.
[16] C. González-Montellano, A. Ramirez, E. Gallego, F. Ayuga, Validation and experimental calibration of 3D discrete element models for the simulation of the discharge flow in silos, Chem. Eng. Sci. 66 (21) (2011) 5116–5126.
[17] D. Höhner, S. Wirtz, V. Scherer, A numerical study on the influence of particle shape on hopper discharge within the polyhedral and multi-sphere discrete element method, Powder Technol. 226 (2012) 16–28.
[18] S. Liu, Z. Zhou, R. Zou, D. Pinson, A. Yu, Flow characteristics and discharge rate of ellipsoidal particles in a flat bottom hopper, Powder Technol. 253 (2014) 70–79.
[19] P. Xu, X. Duan, G. Qian, X. Zhou, Dependence of wall stress ratio on wall friction coefficient during the discharging of a 3D rectangular hopper, Powder Technol. 284 (2015) 326–335.
[20] Y. Zhao, S. Yang, L. Zhang, J. Chew, DEM study on the discharge characteristics of lognormal particle size distributions from a conical hopper, AIChE J. 64 (4) (2018) 1174–1190.
[21] Y. Yu, H. Saxén, Discrete element method simulation of properties of a 3D conical hopper with mono-sized spheres, Adv. Powder Technol. 22 (3) (2011) 324–331.
[22] Z. Lai, Q. Chen, Characterization and discrete element simulation of grading and shape-dependent behavior of JSC-1A Martian regolith simulant, Granular Matter 19 (4) (2017) 69.
[23] S. Mani, L. Tabil, S. Sokhansanj, M. Roberge, Mechanical properties of corn stover grind, 2003 ASAE Annual Meeting, American Society of Agricultural and Biological Engineers 1 (2003) 2003.
[24] M. Wu, D. Schott, G. Lodewijks, Physical properties of solid biomass, Biomass Bioenergy 35 (5) (2011) 2093–2105.
[25] M. Stasiak, M. Molenda, M. Bańda, E. Gondek, Mechanical properties of sawdust and woodchips, Fuel 159 (2015) 900–908.
[26] D. Potyondy, P. Cundall, A bonded-particle model for rock, Int. J. Rock Mech. Min. Sci. 41 (8) (2004) 1329–1364.
[27] Y. Guo, C. Wassgren, B. Hancock, W. Ketterhagen, J. Curtis, Computational study of granular shear flows of dry flexible fibres using the discrete element method, J. Fluid Mech. 775 (2015) 24–52.
[28] B. Lenaerts, T. Aertsen, E. Tijskens, B. De Ketelaere, H. Ramon, J. De Baerdemaeker, W. Saeys, Simulation of grain–straw separation by discrete element modeling with bendable straw particles, Comput. Electron. Agric. 101 (2014) 24–33.
[29] P. Langston, A. Kennedy, H. Constantin, Discrete element modelling of flexible fibre packing, Comput. Mater. Sci. 96 (2015) 108–116.
[30] T. Leblicq, B. Smeets, S. Vanmaercke, H. Ramon, W. Saeys, A discrete element approach for modelling bendable crop stems, Comput. Electron. Agric. 124 (2016) 141–149.
[31] T. Leblicq, B. Smeets, H. Ramon, W. Saeys, A discrete element approach for modelling the compression of crop stems, Comput. Electron. Agric. 123 (2016) 80–88.
[32] Y. Xia, Z. Lai, T. Westover, J. Klinger, H. Huang, Q. Chen, Discrete element modeling of deformable pinewood chips in cyclic loading test, Powder technology 345 (2019) 1–14.
[33] Y. Guo, Q. Chen, Y. Xia, T. Westover, S. Eksioglu, M. Roni, Discrete element modeling of switchgrass particles under compression and rotational shear, Biomass Bioenergy 141 (2020) 105649.
[34] Y. Guo, Q. Chen, Y. Xia, J. Klinger, V. Thompson, A nonlinear elasto-plastic bond model for the discrete element modeling of woody biomass particles, Powder Technol. 385 (2021) 557–571.
[35] Q. Sun, Q. Chen, Y. Xia, F. Chen, J. Klinger, L. Ding, V. Thompson, Reverse scaling of a bonded-sphere DEM model: Formulation and application to lignocellulosic biomass microstructures, Powder Technol. 409 (2022) 117797.
[36] T. Westover, M. Phanphanich, J. Ryan, Comprehensive rheological characterization of chopped and ground switchgrass, Biofuels 6 (5–6) (2015) 249–260.
[37] T. Westover, Y. Xia, J. Klinger, Understanding and solving biomass feeding and handling challenges, Agricultural Research & Technology: Open Access Journal 16 (2) (2018) 001–003.
[38] D. Ilic, K. Williams, R. Farnish, E. Webb, G. Liu, On the challenges facing the handling of solid biomass feedstocks, Biofuels, Bioprod. Biorefin. 12 (2) (2018) 187–202.
[39] K. Zhou, J. Hou, Q. Sun, L. Guo, S. Bing, Q. Du, C. Yao, An efficient LBM-DEM simulation method for suspensions of deformable preformed particle gels, Chem. Eng. Sci. 167 (2017) 288–296.
[40] J. Rojek, A. Zubelewicz, N. Madan, S. Nosewicz, The discrete element method with deformable particles, Int. J. Numer. Meth. Eng. 114 (8) (2018) 828–860.
[41] D. Cantor, M. Cárdenas-Barrantes, I. Preechawuttipong, M. Renouf, E. Azéma, Compaction model for highly deformable particle assemblies, Phys. Rev. Lett. 124 (20) (2020) 208003.
[42] T.-L. Vu, S. Nezamabadi, S. Mora, Effects of particle compressibility on structural and mechanical properties of compressed soft granular materials, J. Mech. Phys. Solids 146 (2021) 104201.
[43] S. Nezamabadi, M. Ghadiri, J.-Y. Delenne, F. Radjai, Modelling the compaction of plastic particle packings, Computational Particle Mechanics (2021) 1–8.
[44] M. Jiang, F. Zhu, F. Liu, S. Utili, A bond contact model for methane hydrate-bearing sediments with interparticle cementation, Int. J. Numer. Anal. Meth. Geomech. 38 (17) (2014) 1823–1854.
[45] M. Jiang, H. Chen, G. Crosta, Numerical modeling of rock mechanical behavior and fracture propagation by a new bond contact model, Int. J. Rock Mech. Min. Sci. 78 (2015) 175–189.
[46] M. Jiang, T. Jiang, G. Crosta, Z. Shi, H. Chen, N. Zhang, Modeling failure of jointed rock slope with two main joint sets using a novel DEM bond contact model, Eng. Geol. 193 (2015) 79–96.
[47] Y. Guo, C. Wassgren, J. Curtis, D. Xu, A bonded sphero-cylinder model for the discrete element simulation of elasto-plastic fibers, Chem. Eng. Sci. 175 (2018) 118–129.
[48] F. Fleissner, T. Gaugele, P. Eberhard, Applications of the discrete element method in mechanical engineering, Multibody Sys.Dyn. 18 (1) (2007) 81.
[49] H. Hertz, Uber die Beruhrung fester elastischer Korper und Uber die Harte, Verhandlung des Vereins zur Beforderung des GewerbefleiBes, Berlin, 1882, p. 449.
[50] R. Mindlin, Elastic spheres in contact under varying oblique forces, J. Appl. Mech. 20 (1953) 327–344.
[51] A. Di Renzo, F. Di Maio, An improved integral non-linear model for the contact of particles in distinct element simulations, Chem. Eng. Sci. 60 (5) (2005) 1303–1312.
[52] L. Verlet, Computer experiments on classical fluids. I. Thermodynamical properties of Lennard-Jones molecules, Phys. Rev. 159 (1) (1967) 98.
[53] Y. Chung, Discrete element modelling and experimental validation of a granular solid subject to different loading conditions, University of Edinburgh, 2006, Ph.D. thesis.
[54] Itasca Consulting Group Inc, PFC – Particle Flow Code, Ver. 5.0, Minneapolis: Itasca, 2014.
[55] C. Kloss, C. Goniva, A. Hager, S. Amberger, S. Pirker, Models, algorithms and validation for opensource DEM and CFD–DEM, Progress in Computational Fluid Dynamics, an International Journal 12 (2–3) (2012) 140–152.
[56] F. Chen, Y. Xia, J.L. Klinger, Q. Chen, A set of hysteretic nonlinear contact models for DEM: Theory, formulation, and application for lignocellulosic biomass, Powder Technol. 399 (2022) 117100.
[57] F. Chen, Y. Xia, J. Klinger, Q. Chen, Hopper discharge flow dynamics of milled pine and prediction of process upsets using the discrete element method, Powder Technol. 415 (2023) 118165.
[58] A. Hamed, Y. Xia, N. Saha, J. Klinger, D.N. Lanning, J. Dooley, Flowability of Crumbler rotary shear size-reduced granular biomass: An experiment-

informed modeling study on the angle of repose, Frontiers in Energy Research (2022) 319.
[59] W. Jin, Y. Lu, F. Chen, A. Hamed, N. Saha, J. Klinger, S. Dai, Q. Chen, Y. Xia, On the fidelity of computational models for the flow of milled loblolly pine: A benchmark study on continuum-mechanics models and discrete-particle models, Frontiers in Energy Research 10.
[60] J.-P. Plassiard, N. Belheine, F.-V. Donzé, A spherical discrete element model: calibration procedure and incremental response, Granular Matter 11 (5) (2009) 293–306.
[61] S. Chehreghani, M. Noaparast, B. Rezai, S. Shafaei, Bonded-particle model calibration using response surface methodology, Particuology 32 (2017) 141–152.
[62] C. Coetzee, Calibration of the discrete element method, Powder Technol. 310 (2017) 104–142.
[63] J. Härtl, J. Ooi, Experiments and simulations of direct shear tests: porosity, contact friction and bulk friction, Granular Matter 10 (4) (2008) 263.
[64] M. Lu, G. McDowell, The importance of modelling ballast particle shape in the discrete element method, Granular matter 9 (1–2) (2007) 69.
[65] N. Guo, J. Zhao, A coupled FEM/DEM approach for hierarchical multiscale modelling of granular media, Int. J. Numer. Meth. Eng. 99 (11) (2014) 789–818.
[66] D.H. Tsai, The virial theorem and stress calculation in molecular dynamics, J. Chem. Phys. 70 (3) (1979) 1375–1382.
[67] G. Baxter, R. Behringer, Cellular automata models of granular flow, Phys. Rev. A 42 (2) (1990) 1017.
[68] D. Walker, An approximate theory for pressures and arching in hoppers, Chem. Eng. Sci. 21 (11) (1966) 975–997.
[69] G. Baxter, R. Behringer, T. Fagert, G. Johnson, Pattern formation in flowing sand, Phys. Rev. Lett. 62 (24) (1989) 2825.
[70] R. Nedderman, Statics and kinematics of granular materials, Cambridge University Press, Cambridge, 1992.
[71] W. Beverloo, H. Leniger, J. Van de Velde, The flow of granular solids through orifices, Chem. Eng. Sci. 15 (3–4) (1961) 260–269.